



Upgrading of bio-liquids on different mesoporous silica-supported CoMo catalysts

R. Nava ^a, B. Pawelec ^{b,*}, P. Castaño ^c, M.C. Álvarez-Galván ^b, C.V. Loricera ^b, J.L.G. Fierro ^b

^a División de Investigación y Posgrado, Facultad de Ingeniería, Universidad Autónoma de Querétaro, Cerro de las Campanas, 76000, Querétaro, Mexico

^b Instituto de Catálisis y Petroleoquímica, CSIC, c/Marie Curie, 2, Cantoblanco, 28049 Madrid, Spain

^c Universidad del País Vasco, Dpto. Ingeniería Química, Apdo 644, 48080 Bilbao, Spain

ARTICLE INFO

Article history:

Received 2 April 2009

Received in revised form 6 July 2009

Accepted 15 July 2009

Available online 22 July 2009

Keywords:

Supported CoMo catalyst

Hydrodeoxygenation

Bio-liquids

Mesoporous silicates

ABSTRACT

Bio-liquids upgrading via catalytic hydrotreating represents an alternative route to produce liquid hydrocarbon fuels. In this paper, the upgrading of an olive oil production-derived by-product has been conducted in a down-flow fixed-bed reactor at 250 °C, 3 MPa with sulfided CoMo catalysts. The catalysts were prepared by successive impregnation (with Mo being introduced first) and supported on different mesoporous silicates (DMS-1, SBA-15, SBA-16, HMS) with the aim to study the effect of support morphology on the catalytic response of sulfided CoMo catalysts. The supports and/or calcined catalysts were characterized by N₂ adsorption-desorption isotherms, XRD, TPR and TPD-NH₃ techniques. In addition, spent catalysts were studied by XPS, HRTEM and TPO/TG techniques. All sulfide CoMo catalysts were stable for 5 h of time-on-stream (TOS) reaction and recorded higher activity than a commercial sulfide NiMo/Al₂O₃ catalyst. The catalysts supported on the SBA-15, SBA-16 and DMS-1 materials were much more effective for oxygen removal than the HMS-supported one. The enhancement of activity was explained in terms of higher active phase exposure and increased acidity. It was found that support morphology affected the distribution of useful products. Considering the balance of desirable and undesirable products, the CoMo/SBA-16 catalyst had an optimal performance.

© 2009 Elsevier B.V. All rights reserved.

1. Introduction

Transportation fuels derived from renewable sources are potentially good alternatives for conventional fossil-derived fuels. This is because the availability of biomass-derived products in countries with no fossil fuels and the low sulfur and metal content of vegetable oils contribute to the neutrality of produced CO₂ [1]. In this respect, the European Community has a target for biofuel use that will substitute 5.75% of transportation fuel by 2010 [2]. Thus, there is now a great interest in the catalytic conversion of bio-oils into gasoline and diesel range hydrocarbons that are low in sulfur and nitrogen [3,4]. Accordingly, the by-products from olive oil production in Spain have a range of potential applications.

In contrast to petroleum-derived feedstocks, bio-liquids contain large amounts of O-containing compounds, i.e. carboxylic acids, esters, aliphatic and aromatic alcohols, ethers, ketones, and aldehydes. As a consequence of such composition, the biomass possesses high viscosity, non-volatility, poor heating value, corrosiveness, immiscibility with fossil fuels, thermal instability, and a tendency to polymerize during storage and transportation [5,6]. Moreover, there is an undesirable formation of carbon

deposits in parts of automotive engines upon combustion (especially, in compression-ignition engines, i.e. diesel engines). Bio-liquids therefore need to be upgraded by reducing their oxygen content.

This means that oxygen should be removed from bio-liquids via hydrotreatment in a petroleum refinery infrastructure. The catalysts commonly used for hydrotreatment are sulfide CoMo/Al₂O₃ and NiMo/Al₂O₃ systems [7]. In literature, liquid fuel production by low-severity hydrotreating of biocrude over NiMo/alumina (Haldor Tøpsøe TK-751) and CoMo/spinel catalysts was reported by Elliott and Neuenschwander [8]. In contrast to the former, the test with the latter showed a dramatic effect of lower catalyst activity. This is because without a strong hydrotreating catalyst effect in the reactor, exothermic pyrolysis condensation reactions cause major temperature excursions and lead to coke buildup on the catalyst surface [8].

Considering the key role of the support morphology, mesoporous silicate materials with ordering pore structure have recently been intensively studied. In particular, mesoporous structures of the MCM-41 family with hexagonal ordering of the pores have attracted widespread attention as new potential materials for the preparation of novel supported hydrotreating catalysts [9–14]. For example, the mesoporous aluminosilicates Al-MCM-41 were found to be very active in the catalytic cracking of palm oil toward the production of gasoline [15,16] and for the pyrolysis of

* Corresponding author. Tel.: +34 915854949; fax: +34 915854760.

E-mail address: bgarcia@icp.csic.es (B. Pawelec).

biomass [17,18]. MCM-41 possesses very interesting textural properties (high specific surface area in the 600–1000 m²/g range and homogeneous pore diameters from 1.5 to 10 nm) [19], which are required when bulkier molecules need to be processed. Furthermore, their high surface area favors active phase dispersion, and a lower strength of acidic OH groups than those in zeolites leads to lower coke formation. Subsequent to MCM-41, the synthesis of another hexagonal mesoporous sieve such as HMS was reported [20,21]. However, the more remarkable advance in the synthesis of mesoporous materials was the preparation of SBA-15, with enhanced thermal and hydrothermal stability with respect to MCM-41 due to the formation of thicker walls (typically between 3 and 9 nm) [22]. SBA-15 material, which has hexagonal pores in a 2D array with long 1D channels (*P6mm* plane group) [23], proved to be effective for supporting CoMo hydrotreating catalysts [9,10]. Another material employed in this work as support was SBA-16. This material was initially synthesized by Zhao et al. [22] in the presence of triblock copolymer Pluronic F127. Contrary to SBA-15, a cubic (*Im3m*) cage-structured mesoporous silica material (SBA-16) is scarcely used as support for hydrotreating catalysts [24,25] although both SBA-15 and SBA-16 materials were stable in boiling water for 48 h [26]. In the SBA-16 material, each mesopore in its body-centred structure is connected to its eight nearest neighbors [27]. This allows easier diffusion of large molecules into pores [24]. Finally, disordered mesoporous silica (DMS-1) was selected in order to compare its morphology with that of materials with hexagonal and cubic mesoporous silica structures (HMS, SBA-15 or SBA-16). DMS-1 has the disordered arrangement of its micropores with high surface area (in the 600–1000 m²/g range) while the atomic arrangement is disordered in a similar manner to the mesoporous silica [28]. However, to date, the application of the DMS-1 material as support for the CoMo hydrotreating catalyst for the HDO of bio-liquids has not been reported.

In this paper, we compare for the first time the catalytic behavior of the sulfided CoMo catalysts supported on DMS-1, SBA-15, SBA-16 and HMS materials in bio-liquids upgrading by hydrotreating. The objective was to study the effect of support morphology on catalytic activity and active phase dispersion. The oxide precursors and spent catalysts were characterized by various techniques (N₂ adsorption–desorption, XRD, DRS, TPR, TPD-NH₃, XPS, HRTEM, and TPO/TGA) and their activity was compared with that of a commercial NiMo/Al₂O₃ catalyst.

2. Experimental

2.1. Support preparation

The siliceous mesoporous SBA-15, SBA-16 and DMS-1 materials were synthesized according to the procedure described by Flodström and Alfredsson [29]. SBA-15 was prepared by using Pluronic triblock copolymer (BASF, EO₂₀-PO₇₀-EO₂₀, P123) as the structure-directing agent, whereas the preparation of DMS-1 and SBA-16 involved different concentrations of Pluronic F127. In all cases, tetraethyl orthosilicate (TEOS, purity 98%, Aldrich) was used as a silica source. In a typical synthesis, the triblock copolymer was dissolved in a solution of water and HCl under stirring, and then the required amount of TEOS was added to the above solution at 35 °C and kept under stirring for 24 h. The mixture was then transferred into polypropylene bottles and heated at 85 °C for 24 h in static conditions. After synthesis, the solid obtained was filtered, thoroughly washed with distilled water, dried at 100 °C and finally calcined at 500 °C for 6 h to remove the organic template.

The HMS molecular sieve was prepared at room temperature by the procedure suggested by Zhang et al. [30] using TEOS (purity 98%, Aldrich) as the neutral silica precursor and dodecylamine (DDA, purity 98%, Aldrich) as the neutral structure director.

Mesitylene (MES, purity 97%, Aldrich) was used as a swelling agent. Briefly, the surfactant (DDA) and the corresponding amount of water were mixed under vigorous stirring to obtain a homogeneous solution. MES was added to the surfactant solution and stirred for 15 min. TEOS was then added to the surfactant-auxiliary solution and the mixture was allowed to react under stirring at room temperature for about 20 h. As the pH increases during the synthesis, the pH of the gel was adjusted several times using acids in order to obtain hydrothermally stable mesoporous silica materials [31]. After synthesis, the solid residue obtained was filtered, thoroughly washed with distilled water and dried in air. Consequently, the sample was dried at 373 K in air for 24 h and finally calcined at 813 K in air for 6 h.

2.2. Catalyst preparation

The respective support was loaded with molybdenum (10 wt%) and cobalt (3 wt%) by incipient wetness successive impregnation (Mo being introduced first) from solutions of ammonium heptamolybdate tetrahydrate (Aldrich, A.C.S. reagent) and cobalt(II) nitrate hexahydrate (purity 98%, Aldrich) to achieve a Co:Mo molar ratio of 1:3. After impregnation, the samples were dried overnight at 110 °C in air and then calcined for 3 h at 500 °C in air. The catalysts are coded as CoMo/SBA-15; CoMo/SBA-16, CoMo/HMS and CoMo/DMS-1.

2.3. Characterization techniques

2.3.1. Chemical analyses

Co and Mo contents were determined using an X-ray fluorescence (TXRF EXTRA-II, Rich & Seifert, Germany) spectrometer.

2.3.2. N₂ adsorption–desorption isotherms

Specific surface areas and pore diameters were determined from the nitrogen adsorption/desorption isotherms, recorded at –196 °C using an Autosorb 1 (Quantachrome) device. Before the physical adsorption measurements, the samples were degassed under argon flow at 473 K for 2 h. Pore size distribution was obtained from the desorption isotherm following the BJH method. The mean standard deviation for the specific surface area measurements was about 2%. The normalized *S*_{BET} (*NS*_{BET}) was calculated from the equation:

$$NS_{BET} = S_{BET} \text{ of catalyst} / [(1 - y) \times S_{BET} \text{ of catalyst}] \quad (1)$$

where *y* is the total Co and Mo content (wt%).

2.3.3. X-ray diffraction (XRD)

Power X-ray diffraction patterns were measured on a DMAX 2100 Rigaku diffractometer. The diffraction patterns were recorded using CuK α radiation in the 2 θ range of 0.5–80°. The assignment of the various crystalline phases was based on the JSPDS powder diffraction file cards. The metal particle sizes were calculated from the line broadening of the most intense peak using the Debye–Scherrer equation.

2.3.4. Temperature-programmed reduction (TPR)

TPR experiments were conducted on a Micromeritics 2900 apparatus provided with a TCD and interfaced to a data station. Prior to reduction, the calcined catalysts (ca. 50 mg) were heated at a rate of 15 °C/min to a final temperature of 400 °C, and kept for 2 h at that temperature under a He flow to remove water and other contaminants. The catalysts were cooled to ambient temperature in the same flow of He; being then reduced in flowing gas containing 10 vol% H₂ in Ar at a total flow rate of 50 mL/min, and

finally heated at a rate of 15 °C/min to a final temperature of 1050 °C.

2.3.5. Temperature-programmed desorption of NH₃ (TPD-NH₃)

The acidity of the plain supports (SBA-15, SBA-16, HMS and DMS-1) was determined by temperature-programmed desorption (TPD) of ammonia. The measurements were carried out with the same apparatus described for TPR. After loading, the sample of 0.050 g was pretreated in a He (Air Liquide, 99.996%) stream at 110 °C for 1 h. Following this, the sample was cooled to 200 °C and ammonia-saturated in a stream of 5% NH₃/He (Air Liquide) flow (50 mL/min) for 1 h. After catalyst equilibration in a helium flow at 120 °C for 0.5 h, the ammonia was then desorbed using a linear heating rate of 10 °C/min to 830 °C. In order to determine the total acidity of the catalyst from its NH₃ desorption profile, the area under the curve was integrated. A semi-quantitative comparison of acid site strength distribution was achieved by Gaussian deconvolution of the peaks. Weak and strong acidities were defined as the areas under the peaks at the lowest and highest temperatures, respectively.

2.3.6. TEM measurements

HRTEM microscopy studies were carried out using a JEM 2100F microscope operating with a 200 kV accelerating voltage and fitted with an INCA X-sight (Oxford Instruments) energy dispersive X-ray microanalysis (EDX) system to verify the semi-quantitative composition of supported phases. The spent CoMo/SBA-15 and CoMo/SBA-16 catalysts were ground into a fine powder and dispersed ultrasonically in hexane at room temperature. A drop of the suspension was then deposited on a lacey carbon-coated Cu grid. At least 10 representative images were taken for each sample. In order to obtain statistically reliable information, the length of ca. 200 particles was measured.

2.3.7. X-ray photoelectron spectroscopy (XPS)

X-ray photoelectron spectra of the spent catalysts were recorded in order to study the effect of the support on active phase dispersion and the degree of sulfidation of the supported species. A VG Escalab 200R spectrometer equipped with a hemispherical electron analyzer and an Mg K α ($\hbar\nu = 1253.6$ eV) X-ray source was used. The samples were first placed in a copper holder mounted on a sample-rod in the pretreatment chamber of the spectrometer and then degassed at 130 °C for 1 h before transfer to the analysis chamber, where residual pressure was kept below 7×10^{-9} mbar during data acquisition. The binding energies (BE) were referenced to the C 1s peak (284.9 eV) to compensate for the charging effects. The areas of the peaks were computed after fitting of the experimental spectra to Gaussian/Lorentzian curves and removal of the background (Shirley function). Surface atomic ratios were calculated from the peak area ratios normalized by the corresponding atomic sensitivity factors [32].

2.3.8. Coke content measurements

Deposited coke was measured by temperature-programmed combustion, performed on a thermogravimetric TGA/SDTA851 device (Mettler Toledo), measuring the weight change in the coked catalysts during oxidation. Each sample (ca. 30 mg) was previously heated to 500 °C for 1 h in N₂ (100 mL/min flow-rate) in order to homogenize coke and remove the volatile compounds. Once the sample had been cooled to 295 °C, a 20% O₂/N₂ gas mixture (62.7 mL/min) was introduced into the analysis chamber and coke was burnt (temperature ramp: 10 °C/min up to 800 °C).

2.3.9. Feedstock

The feedstock used for catalyst activity evaluation was a by-product from olive oil production in Spain. Its elemental

Table 1
Chemical composition of the feedstock^a.

Compound	Formula	(wt%)
2-Phenylhydrazinecarboxamide	C ₇ H ₉ N ₃ O	61.66
9-Hexadecanoic acid	C ₁₆ H ₃₀ O ₂	18.83
Octadecanoic acid	C ₁₈ H ₃₆ O ₂	7.85
Undecane	C ₁₁ H ₂₄	2.47
Palmitic acid	C ₁₆ H ₃₂ O ₂	2.24
Nonane	C ₉ H ₂₀	1.35
Oxacyclotetradecan-2-one	C ₁₃ H ₂₄ O ₂	1.12
Oleic acid, 3-hydroxypropyl ester	C ₂₁ H ₄₀ O ₃	0.67
Octadecanoic acid, 2-hydroxy-1,3-propanediyl ester	C ₃₉ H ₇₆ O ₅	0.45
Benzene, 1,2,3(4)-trimethyl-	C ₉ H ₁₂	0.45
Naphthalene, decahydro-, trans/cis	C ₁₀ H ₁₈	0.22
Spiro[4.5]decane	C ₁₀ H ₁₈	0.22
Nonane, 2-methyl-	C ₁₀ H ₂₂	0.22
Silane, trimethyl[5-methyl-2-(1-methylethyl)phenoxy]-	C ₁₃ H ₂₂ OSi	0.22
(6Z,9Z)-6,9-Pentadecadien-1-ol	C ₁₅ H ₂₈ O	0.22
Hexadecane	C ₁₆ H ₃₄	0.22
Palmitic acid, tetradecyl ester	C ₃₀ H ₆₀ O ₂	0.22
Stearic acid hydrazine	C ₁₈ H ₃₈ N ₂ O	0.22
Linolin, 2-mono-	C ₂₁ H ₃₈ O ₄	0.22
Stearic anhydride	C ₃₆ H ₇₀ O ₃	0.22
1-Heptatriacanol	C ₇ H ₁₆ O	0.22
[(1,4-Diethylcetyl)oxy](trimethyl)silane	C ₁₅ H ₃₄ OSi	0.22
2-Amino-4,4,6,6-tetramethyl-4,6-dihydro-thieno[2,3-c]furan-3-carbonitrile	C ₁₁ H ₁₄ N ₂ OS	0.22
Mass balance	—	98.4

^a By-product from olive oil production in Spain.

composition is the following: C: 75.9%; H: 11.8%; O: 12% (the latter was calculated by difference); N: < 0.1%, S: < 0.1% and traces of Cl. The C, H and N contents were determined by CHN-600 (LECO), whereas the S content was determined by SC132 (LECO) apparatus. The heating value of bio-liquid was 9287 cal/g, as determined by AC300 (LECO) calorimetric pump. In order to decrease feedstock density (0.901 g/mL at 30 °C), the bio-liquid was diluted in n-decane to obtain a 5 vol% solution (density of 0.772 g/mL). Weight content of solvent in the mixture (bio-liquid + solvent) was of 55.5 wt%. This value was selected in order to minimize the concentration gradients over the catalytic bed, thus decreasing the impact of mass and heat transfer limitations.

As expected, the composition of feedstock was complex (Table 1). Bio-liquid (as received) simulated distillation was performed with a Varian CP 3800 GC device using Simulated Distillation Software (STAR SIMDIST) and a capillary column with a length of 10 m and a diameter of 0.53 mm. This analysis method gives the amounts of product in terms of lumps of boiling ranges. Fig. 1(a) and (b) shows the typical chromatogram and boiling-point distribution, respectively. As seen in Fig. 1(b), as received bio-liquid did not have compounds in the gasoline range (C₅: T < 215 °C) and possesses mainly compounds in the range of light cycle oil (LCO: T = 215–325 °C) and heavy cycle oil (HCO: T > 325 °C). The latter has been divided up further into four fractions: light heavy cycle oil (10% LHC₀: 325–360 °C), fatty acids (35% FA: 360–400 °C), intermediates (13% INT: 400–520 °C), and triglycerides (36% TGL: T > 520 °C) [3].

2.3.10. Catalytic activity measurements

The hydroconversion of the bio-liquid was performed in a high-pressure laboratory-scale set-up equipped with a down-flow fixed-bed catalytic reactor. The feedstock mixture (bio-liquid + solvent) was injected (0.25 mL/min) by a high-pressure pump (HPLC Knauer) into a hydrogen stream (60 mL/min). The reaction was carried out at 250 °C, 3 MPa of total pressure, H₂ flow-rate = 7 L (STP) h⁻¹, WHSV_{bio-liquid} = 2.7 h⁻¹ and employing 0.25 g

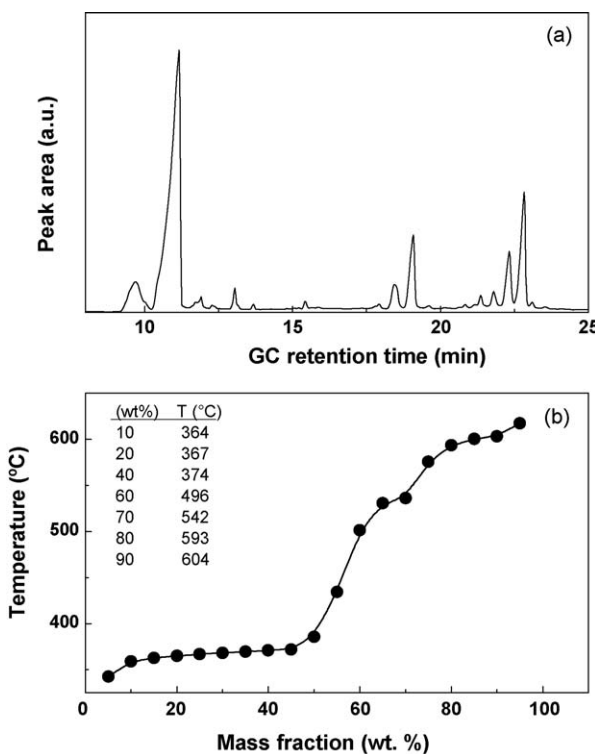


Fig. 1. Simulated distillation chromatogram of the feedstock (a) and the boiling points distribution (b), as obtained from the bio-liquid simulated distillation.

of the catalyst diluted with 5 g of SiC. Before catalyst activation, the catalyst was dried under a N_2 flow of 100 mL/min at 150 °C for 0.5 h. The catalyst was then sulfided in situ at 400 °C and atmospheric pressure by a mixture of 10 vol% of a $H_2S:H_2$ at a rate of 60 mL/min for 4 h (isothermal). After sulfidation, the catalyst was purged under a N_2 flow of 100 mL/min at 400 °C for 0.5 h and then stored overnight under a N_2 flow of 3 mL/min. Before the experimental runs, the N_2 pressure was increased to the desired value, and the catalytic bed was heated to the reaction temperature. GC-MS (Shimadzu GCMS-QP2010) equipped with a Tracer TRB1-MS capillary column (30 m and i.d. 0.32 mm; a 0.10- μ m thick methylsilicone layer; material: fused-silica) was used to identify the components of the reaction mixture. For the calculation of product distribution, it was assumed that the percentage of peak area of the GC-MS chromatogram is linear with compound concentration. Indeed, there are literature reports in which an estimation of organic composition of bio-liquids was based on the peak areas of GC/MS chromatograms (the percentage area of the GC-MS chromatogram was considered linear with the compound concentration) [17,33]. A commercial NiMo/Al₂O₃ catalyst (HR-348 from Procatalyse; $S_{BET} = 164 \text{ m}^2/\text{g}$; and Mo, Ni,

and P loading of 10.7, 2.5, and 2.64 wt%, respectively) was used as a reference.

3. Results and discussion

3.1. Characterization of the oxide precursors

All catalysts were prepared by the incipient wetness impregnation (pore-filling method), with Mo being introduced first (successive impregnation method). According to this method, the deposition of metal precursors takes place mainly in the drying step via precipitation in the bulk solution (*bulk precipitation*) leading to a relatively low dispersion of the supported phases after catalyst calcination [34]. The final metal oxide loading of the catalysts compiled in Table 2 differs from the nominal one probably because the complex mechanism of incipient wetness impregnation when supports with different morphology are employed. Chemical analysis of the calcined catalysts indicates that CoMo/SBA-15 and CoMo/DMS-1 catalysts record the lowest and highest metal oxide loading, respectively. For all catalysts, cobalt oxide loading varies within 2.2–4.7 wt% range, whereas for molybdenum oxide it ranges from 6.4 to 10.1 wt%.

Since the goal of this research was to determine the effect of support in bio-liquid upgrading over supported CoMo catalysts, a detailed characterization of the calcined catalysts was conducted by means of nitrogen adsorption–desorption isotherms, with the aim being to visualize the differences in the support morphologies (Fig. 2). According to IUPAC classification, the N_2 adsorption–desorption isotherm of all the oxide precursors are of type IV [35]. The shape of this isotherm is characteristic of mesoporous materials with a narrow pore size distribution. The isotherm shows a small desorption step at ca. $P/P_0 = 0.4$ originating from ink-bottle-type pores. The nitrogen isotherm of the CoMo/SBA-15 reveals a hysteresis loop of type H1, which is typical for SBA-15 substrate [23]. Its characteristic two-step desorption branch is due to the silica pores plugging [23]. In contrast with CoMo/SBA-15, both N_2 adsorption–desorption isotherms of CoMo/SBA-16 catalyst are very flat. The H1-type hysteresis loop, which starts at a relative pressure of ca. 0.4, is characteristic of the cage-like structure of the SBA-16 material. The isotherm of this catalyst is similar to that reported in literature for SBA-16 mesoporous material [25]. Finally, both CoMo/DMS-1 and CoMo/HMS catalysts record isotherms extended over a large range of relative pressures, indicating the presence of both mesoporosity and macroporosity. The first hysteresis, which starts at a relative pressure of ca. 0.4, indicates the presence of framework mesoporosity, whereas the second hysteresis loop, which starts at a relative pressure of ca. 0.8, is due to textural interparticle mesoporosity or macroporosity. Thus, in addition to framework-confined porosity, the HMS- and DMS-1-supported catalysts have a complementary porosity (textural porosity). For the DMS-1-supported catalyst, the H1-type hysteresis loop is characteristic of a cage-like structure and/or

Table 2

Chemical analysis^a, textural properties^b and XRD data of the oxide precursors and pure supports^a.

Catalyst	Co (wt%)	Mo (wt%)	S_{BET}	NS_{BET}	V_{total}	d (nm)	$\beta\text{-CoMoO}_4$ size ^b (nm)
CoMo/HMS	4.65	6.94	428 (951)	0.48	0.80 (1.30)	6.6 (5.6)	n.d.
CoMo/SBA-15	2.21	6.37	377 (933)	0.43	0.50 (1.10)	5.9 (4.7)	6.8
CoMo/SBA-16	2.81	7.17	407 (830)	0.52	0.30 (0.50)	3.0 (2.6)	30.3
CoMo/DMS-1	4.30	10.12	320 (730)	0.47	0.55 (0.90)	10.3 (2.4)	24.8

The crystal size of $\beta\text{-CoMoO}_4$ phase, as calculated by Scherrer equation from line at $2\theta = 26.3^\circ$.

^a From TXRF measurements.

^b Data of the pure supports are given in parenthesis. S_{BET} : BET surface area ($\text{m}^2/\text{g}_{\text{support}}$); NS_{BET} : normalized S_{BET} ; V_{total} : adsorption total pore volume (m^3/g); d : average pore diameter (nm) calculated from the adsorption branch of N_2 isotherm.

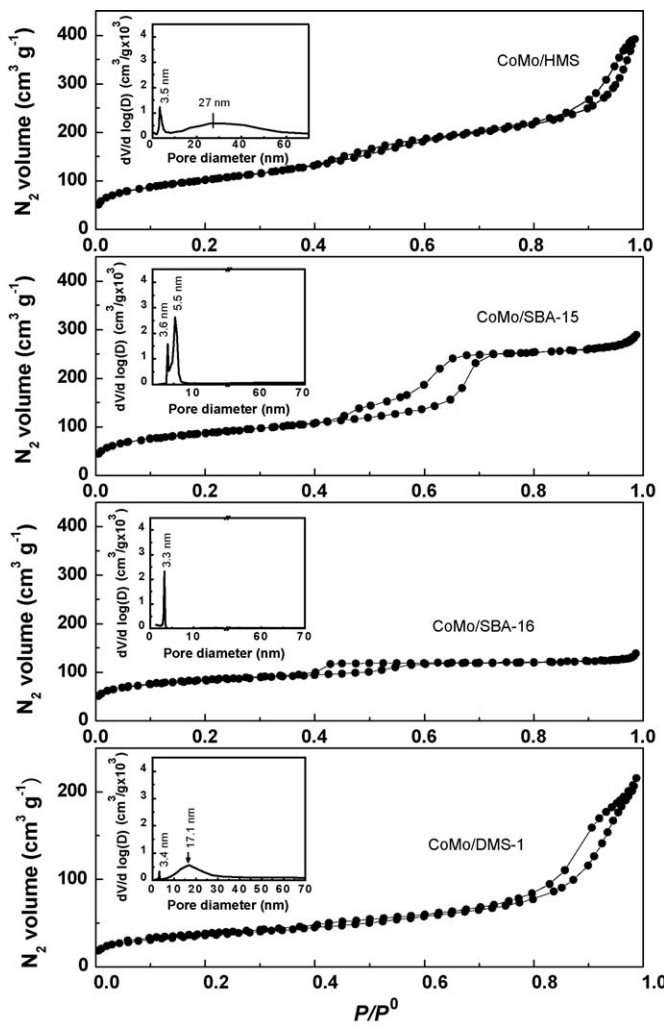


Fig. 2. N₂ adsorption desorption isotherms at 77 K of the calcined CoMo catalysts supported on SBA-15, SBA-16, HMS and DMS-1 materials.

a percolation effect caused by small particles of the metal oxides located within mesopores forming ink-bottle-type pores [36,37].

The pore size distributions of the oxide catalysts, as derived from the desorption branch of N₂ isotherms, are shown in the insets in Fig. 2. The pore size distribution of CoMo/HMS catalyst reveals one narrow peak centred at 3.5 nm (structural mesoporous) and another broad peak centred at 27 nm (textural mesoporous). For the CoMo/SBA-15 sample, the pore size distribution shows two distinct peaks: one located in the pore width range < 4 nm, indicating the presence of small complementary pores (mainly micropores), and a second one of 5.5 nm representing the ordered mesopores [38]. Similarly, the pore size distribution of CoMo/DMS-1 shows the expected bimodal pore system presenting one peak centred at 3.4 nm (structural mesopores) and another peak with a maximum at 17.1 nm (textural mesopores). The CoMo/SBA-16 sample is unique among the catalysts studied, showing a narrow BJH pore size distribution centred at 3.3 nm; its narrow and uniform pore size distribution suggests that the supported species are uniformly distributed.

A clearer view of the occurrence of pore blocking can be obtained by calculating the BET specific areas of oxide CoMo catalysts referred to unit mass of support. The respective values collected in Table 2 show S_{BET} specific areas in the range of 320 m²/g (CoMo/DMS-1) to 428 m²/g (CoMo/HMS), which follows the same trend as total pore volume. By comparing the total and micropore volume of the

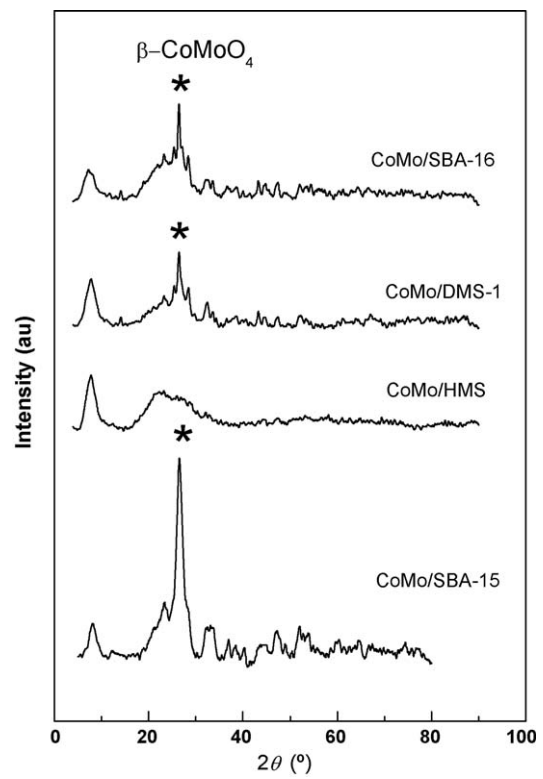
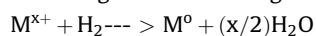


Fig. 3. X-ray diffraction patterns of the calcined CoMo catalysts supported on HMS, SBA-16, SBA-15 and DMS-1 materials.

catalysts and supports (Table 2), it can be inferred that Co and Mo oxides block the substrate pores, mainly the micropores. This is probably the reason for the increase in the average pore diameter after impregnation with CoMo (the microporosity is lost). The normalized specific areas for all catalysts fall in the 0.43–0.52 range, indicating that Mo and Co oxide species are located mainly in the internal pore network of the mesoporous systems.

The wide-angle X-ray diffraction patterns of the calcined catalysts are presented in Fig. 3. The CoMo/HMS sample does not display any diffraction lines due to Co and/or Mo oxide phases. This might indicate that the oxide phases incorporated are either amorphous (or not fully crystalline) or their crystal size is less than 4 nm, so they do not diffract. On the other hand, the XRD patterns of the CoMo/SBA-15 catalyst record a small peak at ca. 23.4° 2θ and another narrow and intense one at 26.6° 2θ ; both assigned to β -CoMoO₄ crystalline phase (JCPDS card 21-868). Using this peak, the crystal size of the β -CoMoO₄ phase, calculated according to Scherrer's equation, is ca. 6.8 nm (Table 2). The same phase was detected when using SBA-16- and DMS-1-substrates. For these systems, only a much less intense peak at 26.3° 2θ is observed, whereas the peak at 23.4° 2θ is not detected. Similar calculations for these CoMo/SBA-16 and CoMo/DMS-1 systems gave crystallite size values of 30.3 and 24.8 nm, respectively, for the β -CoMoO₄ phase (Table 2).

Temperature-programmed reduction (TPR) experiments provide information about the dispersion states of the metal oxides as well as some insights on the metal-support (or Co–Mo) interactions. Fig. 4 displays the TPR profiles of the CoMo phases deposited on HMS, SBA-15, SBA-16 and DMS-1 substrates. The observed hydrogen consumption is related to the reduction of oxide phases according to the following stoichiometry:



where M is either Co or Mo and x is the oxidation state. For all catalysts, TPR profiles show a narrow peak with a maximum at

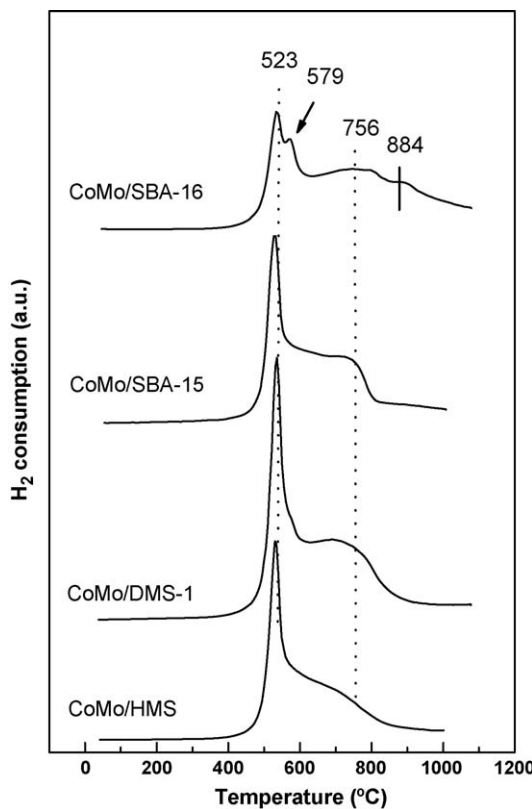


Fig. 4. TPR profiles of the calcined CoMo catalysts supported on different mesoporous silicas.

temperatures in the 450–600 °C range and a broad shoulder extending in the 605–847 °C temperature range. In line with the XRD profiles (*vide supra*) and previous literature reports [39,40], this sharp TPR peak can reasonably be ascribed to a reduction in the CoMoO₄ phase. Since cobalt oxide is reduced more easily than MoO₃, it is likely that free cobalt oxide species also contribute to some extent to that H₂-consumption peak. For the monometallic Co/SiO₂ catalyst, it was shown that the reduction of Co oxide occurs at 360 and 445 °C [41]. However, the somewhat higher reduction temperature observed here is a consequence of the polarization of the Co–O bond by the Mo⁶⁺ ions, which makes it more ionic and consequently more difficult to reduce [41].

Owing to the similarity of the isoelectric points of silica and MoO₃, one may assume that molybdenum forms polymolybdate structures on the silica surface at any loading. Laine et al. [42] assigned the H₂-consumption peak at 756 °C to dispersed polymolybdates linked to the silica surface, while the one located at the highest temperature (884 °C) is most likely due to poorly crystalline MoO₂ generated from the reduction of the MoO₃ phases. After Gaussian deconvolution of the TPR profiles (not shown here), H₂ consumption amounts were calculated by considering the area

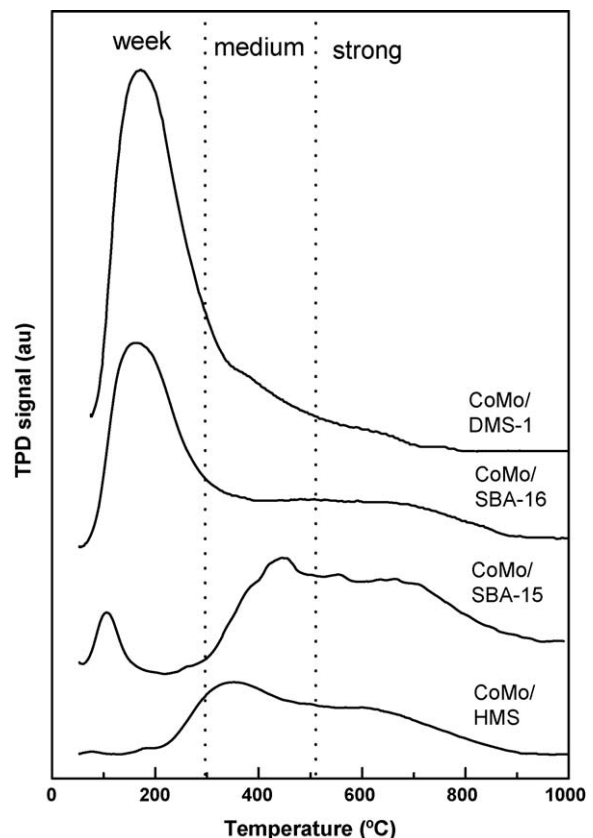


Fig. 5. TPD profiles of NH₃ adsorbed on the calcined CoMo catalysts (normalized to BET surface area).

of the peaks (Table 3). The amounts of H₂ consumed follow the order: CoMo/DMS-1 > CoMo/SBA-16 > CoMo/SBA-15 > CoMo/HMS. It can thus be inferred that a larger quantity of CoMoO₄ phase is formed in the DMS-1 substrate.

Experiments of temperature-programmed desorption of ammonia (TPD-NH₃) were conducted to compare the acidity of these mesoporous silica-supported CoMo catalysts. The TPD-NH₃ profiles of the catalysts normalized to BET surface area (from Table 2) are displayed in Fig. 5. Acidity distribution was derived from experimental TPD curves by fitting to Gaussian lines (not shown here), in which three peaks were used to represent weak (T < 300 °C), medium (300 °C < T < 500 °C) and strong (T > 500 °C) acidity, respectively [43]. As seen in this figure, all catalysts show clear differences in the quantity of weak acid sites (CoMo/DMS-1 > CoMo/SBA-16 ≫ CoMo/SBA-15 ≈ CoMo/HMS (none)). The total acidity and acid distribution of the samples are listed in Table 3, according to NH₃-TPD profiles. CoMo/SBA-15 and CoMo/HMS catalysts show the largest amount of medium and strong acid sites, whereas CoMo/SBA-16 and CoMo/DMS-1 exhibit the largest amount of weak acid sites. The trend in medium and

Table 3
Acid sites distribution^a and H₂ uptake^b for calcined CoMo catalysts^a.

	Acid sites concentration (μmol NH ₃ g _{cat} ⁻¹)				H ₂ uptake (μmol/g _{cat})		
	Weak <300 °C	Medium 300–500 °C	Strong >500 °C	Total	I peak	II peak	Total
CoMo/HMS	0.00	0.38	0.35	0.72	95.8	112.0	207.8
CoMo/SBA-15	0.05	0.81	0.20	1.06	161.0	66.1	227.1
CoMo/SBA-16	0.70	0.46	0.13	1.29	710	190.0	261.0
CoMo/DMS-1	1.22	0.38	0.00	1.61	134.0	178.0	312.0

^a Amount of desorbed ammonia normalized to BET surface area (from Table 1) as determined by TPD of NH₃.

^b As obtained by Gaussian deconvolution of the TPR patterns.

Table 4

Oxygen percentages^a corresponding to different O-containing products before and after bio-liquid HDO ($T = 250^\circ\text{C}$, $P = 3 \text{ MPa}$, $\text{TOS} = 5 \text{ h}$) over supported CoMo catalysts and reference sample^b.

Compound	Feedstock	CoMo/HMS	CoMo/SBA-15	CoMo/SBA-16	CoMo/DMS-1	Ref. ^b
Total oxygen (%)	4.6	0.5	0.1	0.1	0.1	0.5
Hydrozaine carboxamide, <i>N</i> -phenyl- ($\text{C}_7\text{H}_9\text{N}_3\text{O}$) (0%)	2.9	–	–	–	–	–
<i>n</i> -Hexadecanoic acid ($\text{C}_{16}\text{H}_{32}\text{O}_2$) (0%)	0.1	–	–	–	–	–
9-Hexadecanoic acid ($\text{C}_{16}\text{H}_{32}\text{O}_2$) (0%)	1.1	–	0.1	0.1	0.1	–
Octadecanoic acid, octyl ester ($\text{C}_{26}\text{H}_{52}\text{O}_2$) (0%)	0.4	0.2	–	–	–	0.4
Oxacyclotetradecan-2-one ($\text{C}_{13}\text{H}_{24}\text{O}_2$) (0%)	0.1	–	–	–	–	–
Oleic acid ($\text{C}_{18}\text{H}_{34}\text{O}_2$) (0%)	–	0.2	–	–	–	0.1

^a From stoichiometric analysis.

^b A commercial NiMo/Al₂O₃ (HR-348).

strong acidities is similar (CoMo/SBA-15 > CoMo/HMS > CoMo/SBA-16 > CoMo/DMS-1).

3.2. Oxygen removal from bio-liquid

The general aim of this study is to produce O-free bio-liquid with high content of desirable products such as paraffins, olefins, alcohols, ketones and naphthenes. Elemental analysis indicated that total oxygen content in the as-received bio-liquid is ca. 12% (4.56%, as determined by stoichiometric calculation). The bio-liquid upgrading via catalytic hydrotreating over sulfided CoMo catalysts was performed in a down-flow reactor at 250 °C, 3 MPa of total hydrogen pressure and WHSV_{bio-liquid} = 2.7 h⁻¹. The effect of support morphology on catalytic response of sulfided CoMo catalysts supported on HMS, SBA-15, SBA-16 and DMS-1 substrates has been evaluated. A commercial NiMo/Al₂O₃ catalyst was used as reference because it is known that Ni has a higher HYD activity than Co.

The main compounds present in the bio-liquid, as determined by the GC/MS technique, are listed in Table 1. As seen in this table, the feedstock contains mainly 2-phenylhydrazinecarboxamide (61.7 wt%), carboxylic acids (28.8 wt%), a relatively small amount of paraffins (4.3 wt%) and other compounds such as alcohols, ketones, esters, naphthenes, etc. (ca. 5.0 wt%). The carboxylic acids present in the bio-liquid were mainly 9-hexadecanoic acid ($\text{C}_{16}\text{H}_{30}\text{O}_2$; 18.8 wt%), octadecanoic acid ($\text{C}_{18}\text{H}_{36}\text{O}_2$; 7.9 wt%) and palmitic acid ($\text{C}_{16}\text{H}_{32}\text{O}_2$; 2.2 wt%). Phenylhydrazinecarboxamide and carboxylic acids have to be removed from biomass because low pH values mean that they have a corrosive effect on engine parts.

The total oxygen percentages before and after HDO of bio-liquid is shown in Table 4. As seen in this table, the catalysts supported on SBA-15, SBA-16 and DMS-1 substrates were the most effective toward oxygen removal followed by CoMo/HMS. However, 9-hexadecanoic acid still remained after the HDO reaction over three former catalysts, whereas the partial oxygen elimination from octadecanoic acid octyl ester and oleic acid occurs on the latter. In addition, it is emphasised that the commercial NiMo/Al₂O₃ catalyst is not effective for oxygen removal from the octadecanoic acid octyl ester. In general, all supported CoMo catalysts proved to be more active than this reference.

A comparison of catalyst performance and TPD-NH₃ results (Table 3) reveals that lower oxygen content is achieved upon bio-liquid HDO on sulfide CoMo catalysts with a larger amount of acid sites per unit area (CoMo/SBA-15, CoMo/SBA-16, CoMo/DMS-1). The lowest activity for O-removal of CoMo/HMS catalyst could be linked to its lower amount of acid sites. Other factors, which could influence on the catalytic response, are the specific surface area and metal loadings of the catalysts (Table 2). In order to clarify this point, the oxygen content after 5 h on stream was normalized to S_{BET} as well as to metal loadings (Fig. 6(A) and (B), respectively). In both cases, it was found that catalyst activity follows the order: CoMo/DMS-1 ≈ CoMo/SBA-15 ≈ CoMo/SBA-16 ≫ CoMo/HMS > reference cata-

lyst. This might indicate the larger extent of O-removal over the three former catalysts is linked with the active phase dispersion rather than with specific surface area of the catalysts.

3.3. Effect of support morphology on the product distribution

Table 5 compiles the product distribution achieved over all catalysts after 5 h of on-stream reaction. For all catalysts, the 2-phenylhydrazinecarboxamide (main compound of bio-liquid) disappeared completely and a drastic decrease in carboxylic acids occurs being CoMo/SBA-15 and CoMo/DMS-1 catalysts the most effective for their elimination. 9-hexadecanoic acid remained only after the HDO reaction over SBA-15-, SBA-16 and DMS-1-supported catalysts. The octadecanoic acid octyl ester and oleic acid still remained after 5 h of on-stream reaction over CoMo/HMS and reference sample.

Analyzing the products distribution recompiled in Table 5, it is clear that the reactions occurring during bio-liquid hydroprocessing are elimination of nitrogen as ammonia from 2-phenylhydrazinecarboxamide, elimination of oxygen as water, and hydrogenation-hydrocracking of large molecules. According to literature [44], ammonia is a strong inhibitor of all hydrotreating

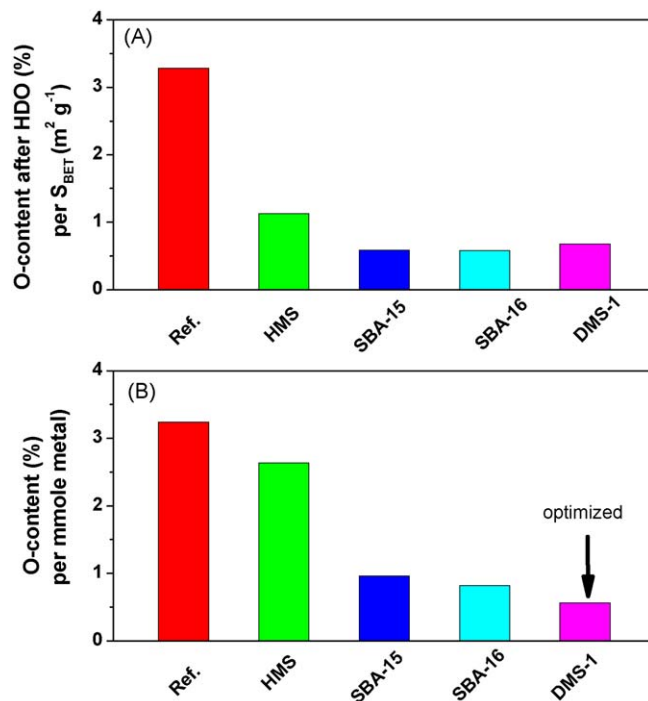


Fig. 6. Influence of support on the total oxygen content after HDO of bio-liquid over sulfided CoMo catalysts ($T = 250^\circ\text{C}$, $P = 3 \text{ MPa}$, $\text{WHSV} = 2.7 \text{ h}^{-1}$, $\text{TOS} = 5 \text{ h}$) normalized to S_{BET} (A) and mmol of Co and Mo (B).

Table 5Product distribution after feedstock's hydrotreatment^a over sulfided catalysts.

Compounds (wt%)	CoMo/HMS	CoMo/SBA-15	CoMo/SBA-16	CoMo/DMS-1	Ref. ^b
Nonane (C_9H_{20})	2.47	1.79	1.79	1.60	3.36
Nonane, 2-methyl- ($C_{10}H_{22}$)	0.22	0.22	0.22	0.22	0.22
<i>n</i> -Decane formed ($C_{10}H_{22}$)	80.27	89.24	62.11	14.57	69.96
Undecane ($C_{11}H_{24}$)	2.69	2.9	2.91	2.91	0.90
Undecane, 2,5-dimethyl- ($C_{13}H_{28}$)	–	–	–	41.26	–
<i>n</i> -Tridecane ($C_{13}H_{28}$)	–	–	–	–	0.22
Pentadecane ($C_{15}H_{32}$)	0.45	–	–	–	1.57
Hexadecane ($C_{16}H_{34}$)	–	0.22	0.22	0.22	1.35
Spiro[4,5]decane ($C_{10}H_{18}$)	–	–	0.22	–	–
1-Hepten-5-yne, 2-methyl-3-methylene- (C_9H_{12})	–	–	0.22	–	–
1-Hexene, 3,4-dimethyl- (C_8H_{16})	–	–	–	24.44	–
(2Z)-2-Benzyl-3-phenyl-2-propenal ($C_{15}H_{12}O$)	0.22	–	–	–	–
9-Octadecanol ($C_{18}H_{34}O$)	–	–	–	–	0.22
Stearaldehyde ($C_{18}H_{36}O$)	–	–	–	–	0.22
Methanol (CH_4O)	–	–	27.13	9.87	–
1-Eicosanol ($C_{20}H_{42}O$)	–	–	0.22	–	–
1-Pentadecanol ($C_{15}H_{32}O$)	–	–	–	–	0.22
1-Octadecanol ($C_{18}H_{38}O$)	–	–	–	–	1.57
9-Hexadecanoic acid ($C_{16}H_{30}O_2$)	–	2.24	2.46	2.24	–
Palmitic acid ($C_{16}H_{32}O_2$)	0.45	0.45	0.45	0.45	0.67
Octadecanoic acid ($C_{18}H_{36}O_2$)	0.90	0.45	0.45	0.45	2.47
Palmitic acid, tetradecyl ester ($C_{30}H_{60}O_2$)	–	–	–	–	0.90
Oleic acid, 3-hydroxypropyl ester ($C_{21}H_{40}O_3$)	0.22	–	–	–	–
Benzene, 1,2,3(4)-trimethyl- (C_9H_{12})	0.22	0.45	0.22	0.45	–
Naphthalene, decahydro-, trans and/or cis ($C_{10}H_{18}$)	1.79	1.12	0.45	0.45	3.14
Mass balance	98.87	99.55	99.77	99.78	98.20

^a Reaction conditions were: $T = 250^\circ C$; $P = 3$ MPa and TOS = 5 h.^b A commercial NiMo/Al₂O₃ (HR-348).**Table 6**

Product distribution after bio-liquid hydrotreatment at TOS = 5 h over sulfided CoMo catalysts and reference sample.

	Feedstock	CoMo/HMS	CoMo/SBA-15	CoMo/SBA-16	CoMo/DMS-1	Reference sample ^b
Desirable (%)						
Paraffins	4.3	86.3	94.4	67.2	60.8	78.5
Olefins	–	–	–	0.2	24.4	–
Alcohols	0.4	–	–	27.4	9.9	1.8
Ketones	1.1	–	–	–	–	–
Naphthenes	0.2	1.8	1.1	0.4	0.4	3.4
Undesirable (%)						
Amine ^a	61.7	–	–	–	–	–
Esters	1.6	5.4	0.4	0.7	0.7	9.2
Aromatics	0.4	1.1	0.4	0.2	0.4	0.2
Acids	28.8	5.2	3.1	3.7	3.1	5.8
Others	1.5	0.2	0.6	0.2	0.3	1.2

^a Hydrozaincarboxamine, *N*-phenyl- ($C_7H_9N_3O$).^b A commercial NiMo/Al₂O₃ (HR-348).

reactions over CoMo and NiMo catalysts but does not affect the hydrogenation of the ketonic groups. On the contrary to ammonia, water has no influence (or very little inhibiting effect) for all reactions except for the promotion of hydrolysis of carboxylic esters. However, one might expect that the use of down-flow reactor could minimize the effect of ammonia.

In order to facilitate understanding of the selectivity trends, the products were grouped in compound families (Table 6). The identified liquid products, grouped into desirable and undesirable groups, are compared in Fig. 7. The group of desirable products contains paraffins, olefins, alcohols and naphthenes, whereas the group of undesirable products includes aromatics, acids and esters, the latter due to their high O-content. Fig. 8 compares the GC-MS signal for all catalysts corresponding to retention time in the range 10–12 min. For comparison, the MS-GC chromatogram of the feedstock (5% of biomass in *n*-decane) is included. As seen in Fig. 8, the $C_{10}H_{18}$ (naphthalene, decahydro-, trans/cis; spiro[4,5]decane) is mainly formed over a commercial NiMo/Al₂O₃ followed by CoMo/HMS and CoMo/SBA-15 catalysts. Irrespective of the support

morphology, the SBA-15-, SBA-16-, DMS-1-supported CoMo catalysts show similar total yields of desirable products, indicating that more complex factors than support morphology affect product distribution on those catalysts. While paraffins are mainly formed on all catalysts, large amounts of olefins and alcohols are formed on the CoMo/DMS-1 and CoMo/SBA-16 catalyst, respectively. The paraffins formation follows the trend: CoMo/SBA-15 > CoMo/HMS > a commercial catalyst > CoMo/SBA-16 ≫ CoMo/DMS-1 (Table 6). The high olefin content (1-hexene, 3,4-dimethyl-; C_8H_{16}) of the CoMo/DMS-1 is in line with the lowest paraffins formation on this catalyst (Table 6). The high formation of 3,4-dimethyl-1-hexene on the CoMo/DMS-1 sample is surprised with a hydrogenation process. Further study is needed in order to explain this phenomenon. On the contrary, high methanol formation in the bio-liquid upgrading over CoMo/SBA-16 sample is not surprising since the direct production of alcohols via acid hydrogenation is well-known over heterogeneous catalysts [45]. Moreover, an analysis of product distribution in Table 5 reveals that CoMo/SBA-16 and the commercial catalyst are the only ones that effectively

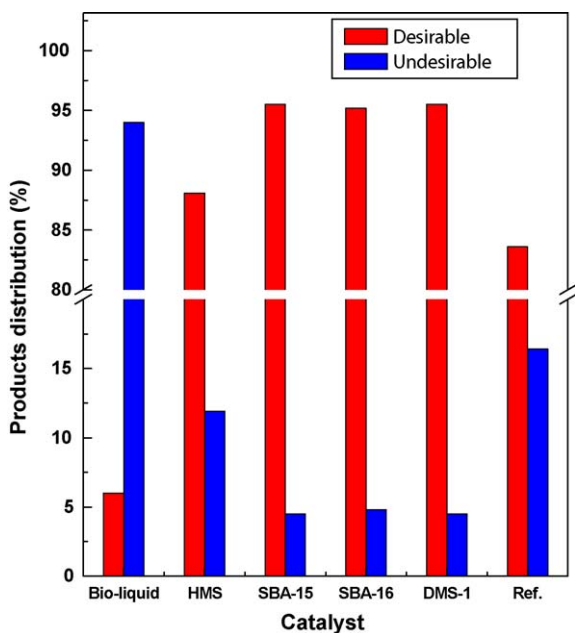


Fig. 7. Distribution of desirable and undesirable products after bio-liquid hydrotreatment at $T = 250^\circ\text{C}$, $P = 3 \text{ MPa}$, TOS = 5 h.

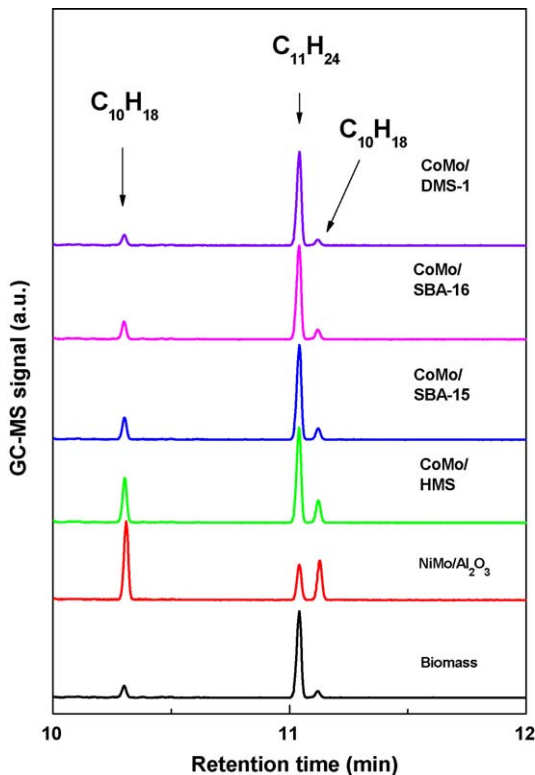


Fig. 8. MS-GC chromatographs corresponding to retention time in range 10–12 min. For comparison, the MS-GC chromatograph of the feedstock is included.

reduce the polycyclic aromatics (PAH), which must be eliminated from bio-liquid because they are considered as hazardous for the environment [46]. PAHs are formed on CoMo/HMS catalyst, whereas the two SBA-15- and DMS-1 counterparts are not at all effective for their reduction.

Finally, one might expect that the course of hydrogenation reaction could be substantially influenced by the type of solvent used (polar or nonpolar) [47]. For the activity test, the bio-liquid

was diluted with *n*-decane (5 vol%). Considering the study by Bejblová et al. [47], it is expected that the use of *n*-decane as solvent led to fast consecutive hydrogenation of aromatic rings of polycyclic aromatic hydrocarbons (PAH), which are present in the feedstock. Moreover, although an inert solvent does not participate in the reaction process, it is expected that it may compete with the reactants for the adsorption on active sites on the catalyst surface [48]. However, in our study no parallel reactions of *n*-decane (hydroisomerization/hydrocracking) were observed. Thus, one might deduce that under reaction condition employed, the competitive adsorption of *n*-decane and bio-liquid's compounds on the active sites did not occur. On the contrary, the *n*-decane was additionally formed due to cracking of the large compounds present in the feedstock (Table 5).

3.4. Catalyst stability during the contact with H_2O

To exclude the deterioration of the porous structure of the catalysts by the water product arising from the HDO reaction, low-angle X-ray diffraction profiles of the spent CoMo/SBA-15 and CoMo/SBA-16 catalysts were recorded (Fig. 9). The most intense XRD lines of spent CoMo/SBA-15 catalyst belong to the hexagonal arrangement of the support pore structure, whereas that of the CoMo/SBA-16 catalyst corresponds to the cubic arrangement of its pores. For the spent CoMo/SBA-15, the half-width of the diffraction peak associated to the (100) plane of the *P6mm* structure (at $2\theta = 1.0$) is wider than the corresponding signal of its calcined precursor. The smaller signals observed in the enlargement of the diffraction profile indicate the presence of some hexagonal order in agreement with the TEM pictures (Fig. 10). As compared with the respective calcined catalysts, the intensity of the XRD peak after

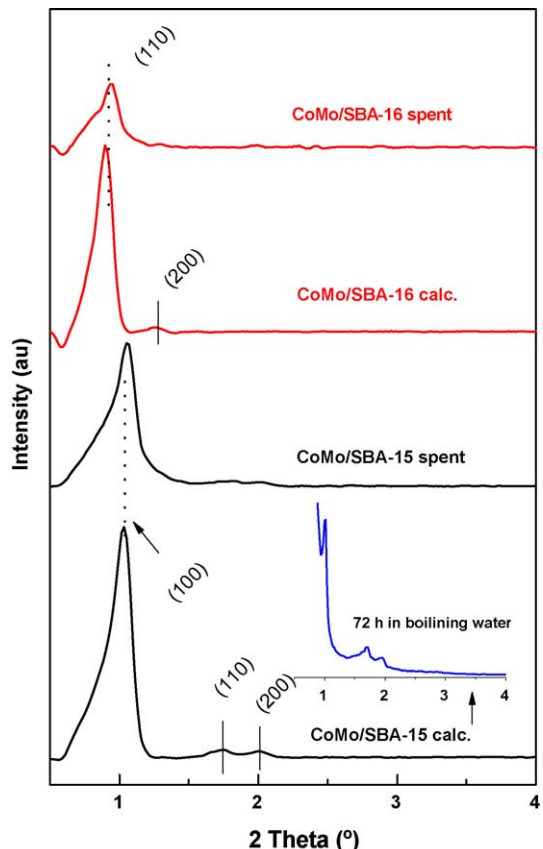


Fig. 9. Low-angle XRD measurements of the calcined and spent CoMo/SBA-15 and CoMo/SBA-16 catalysts. XRD diffractogram of the calcined CoMo/SBA-15 treated with boiling water for 72 h is shown in inlet of this figure.

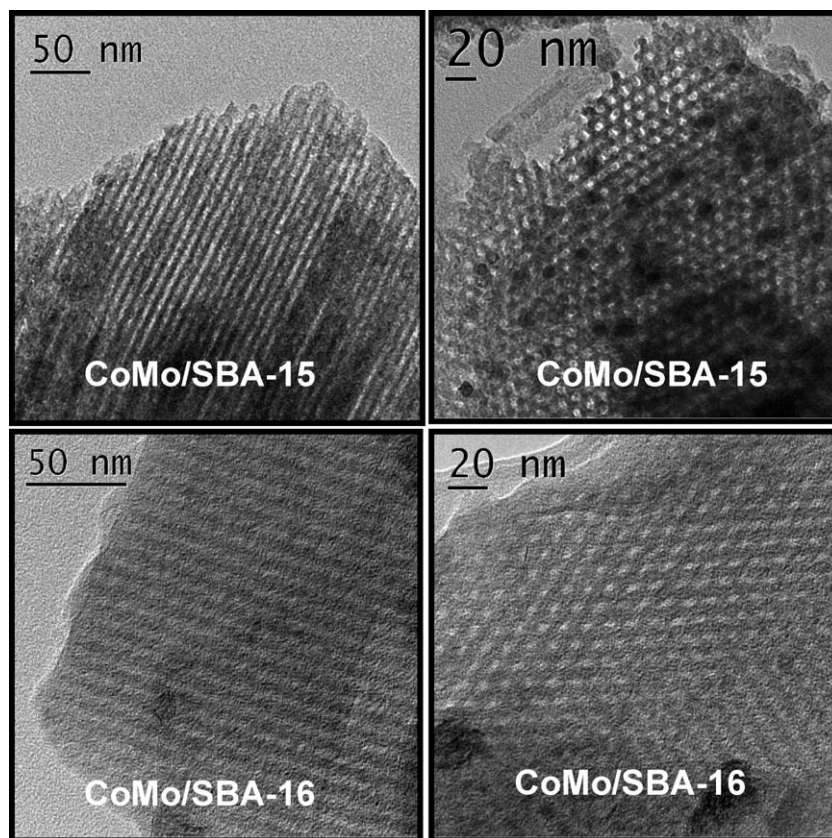


Fig. 10. TEM images of the spent CoMo/SBA-15 and CoMo/SBA-16 catalysts viewed through different orientations.

on-stream reaction decreases, with this decrease being larger for SBA-16 than for SBA-15-supported catalyst. Thus, from these diffraction profiles it can be concluded that both CoMo/SBA-16 and CoMo/SBA-15 catalysts remain stable under the reaction conditions applied. In order to verify the stability of CoMo catalysts supported on mesoporous silica during long time exposure to H₂O, additional experiment was performed in which CoMo/SBA-15 catalyst was exposed to boiled H₂O for 72 h. After this, the catalyst was dried at room temperature for 18 h and then dried at 110 °C for 18 h. A low-angle XRD of this sample (inlet of Fig. 9) confirmed that structure of SBA-15 material was preserved after this long treatment. Similarly, the hydrophobicity of the pure-silica MCM-41 was confirmed by water adsorption experiments by Chen et al. [49]; with temperatures as high as 850 °C in air with 8 mbar water vapour before structure collapse begins.

The stability of the pore structure during on-stream reaction was confirmed also by transmission electron microscopy (TEM). Fig. 10 displays TEM images, viewed at different sample orientations, for spent CoMo/SBA-15 and CoMo/SBA-16 catalysts. The TEM images belonging to CoMo/SBA-15 clearly reveal a 2D-hexagonal pore arrangement and long-range mesoporous-ordering, which is characteristic of the good-quality SBA-15 material. Similarly, the 3D cubic pore arrangement could be inferred for the spent CoMo/SBA-16. Thus, formation of water during on-stream reaction does not alter the regular ordered array of mesopores of both catalysts in agreement with the low-angle XRD data (Fig. 9).

Since the water produced in the HDO reaction may affect the stability of the sulfided catalysts by hydrolyzing the sulfide phases [50], the morphology of the spent CoMo/SBA-15 and CoMo/SBA-16 catalysts was studied by means of transmission electron micro-

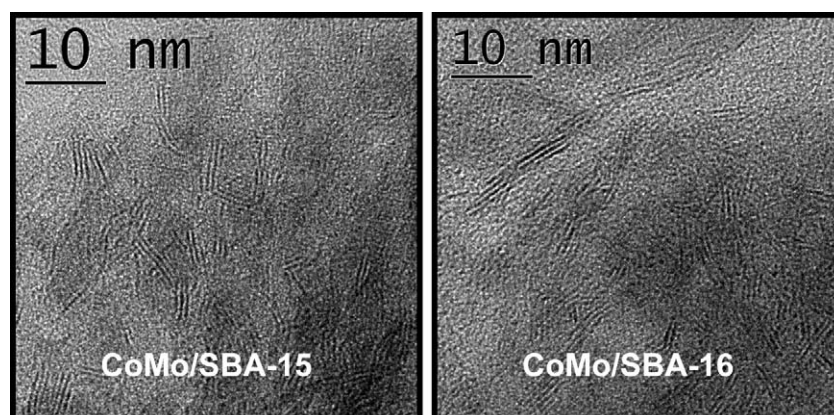


Fig. 11. High magnification of MoS₂ sheets observed with spent CoMo/SBA-15 and CoMo/SBA-16 catalysts.

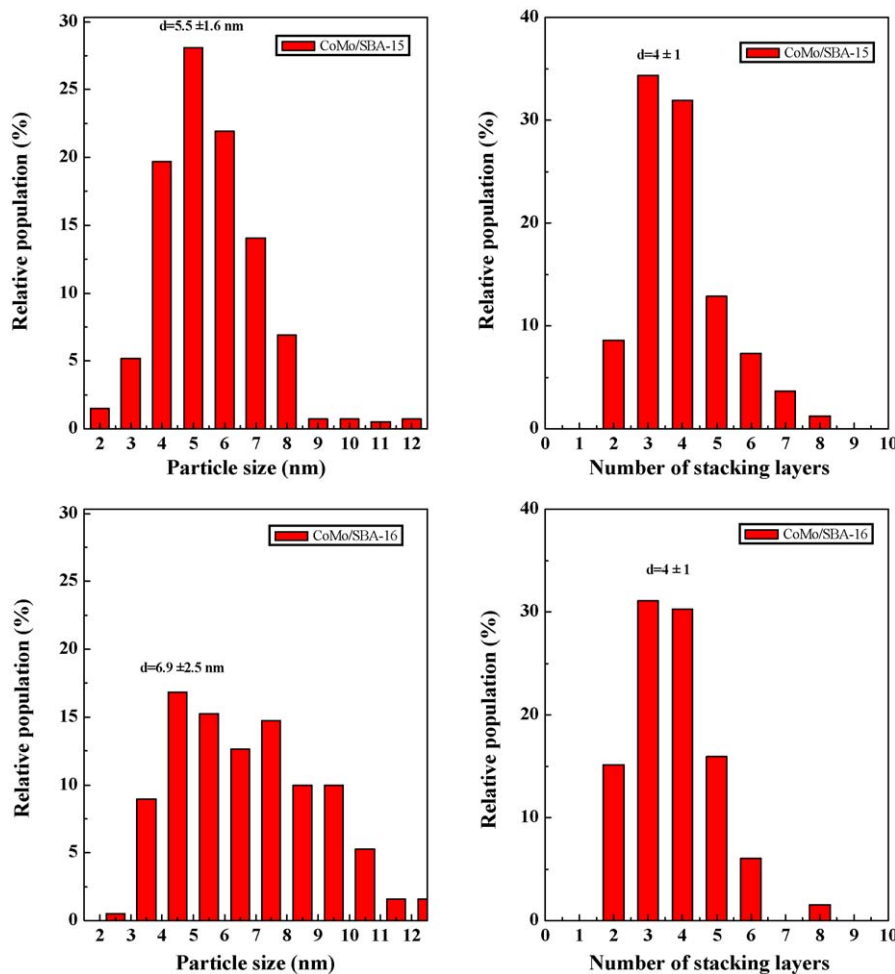


Fig. 12. Histograms of the metal sulfide particle size distribution (left) and stacking layers (right) of the spent CoMo/SBA-15 (top) and CoMo/SBA-16 (bottom) catalysts.

scopy (Fig. 11). TEM micrographs of both samples show MoS_2 particles with a very irregular shape. However, the MoS_2 particles appear to be more homogeneously dispersed in the SBA-15 than in the SBA-16-based catalyst. The number of stacking layers for the spent CoMo/SBA-15 is between 3 and 4, with an average of 2.3 layers. The average slab length is calculated to be 5 nm. On the other hand, the slabs for the spent CoMo/SBA-16 appear heterogeneously distributed. Some nest-like stacks, in which several slabs are cross-linked, were observed in some of the micrographs. The stacks are higher than those in the case of SBA-15-based catalyst and consist of up to 5 layers. The average number of stacking layers is 2.8 and the average slab length is the same as for CoMo/SBA-15. From the distribution of MoS_2 stacking (Fig. 12), higher stacking is observed for the SBA-16-supported catalyst than for its SBA-15-supported counterpart. This indicates a Fig. 13(A) weaker interaction between the SBA-16 support and supported MoS_2 species.

3.5. XPS characterization of spent catalysts

The surface composition and chemical state of the components in spent catalysts were investigated by XPS technique. The BE values of the Si 2p, Mo 3d_{5/2}, Co 2p and S 2p core levels are compiled in Table 7. As an example, the Mo 3d and Co 2p core-level spectra of the spent CoMo/DMS-1 catalyst are shown in Fig. 13(A) and (B), respectively. After on-stream conditions, all the catalysts record Mo 3d_{5/2} binding energies of 229.0 ± 0.1 eV, which are

typical of Mo^{4+} in MoS_2 phase [51]. The S 2p_{3/2} binding energy of 162.0 ± 0.1 eV is characteristic of the S^{2-} -type ligands present in this phase. Irrespectively of the support employed, Mo species are completely sulfided for all catalysts. On the other hand, the Co 2p_{3/2} core-level spectra make two contributions: a minor one at 778.0–778.2 eV characteristic of Co-sulfide species [52], and another at 781.1–781.6 eV belonging to non-sulfided Co species.

Considering the sulfidation degree, the S/(Mo + Co) atomic ratios of the catalysts follow the trend (Table 7): CoMo/HMS > CoMo/DMS-1 > CoMo/SBA-16 > CoMo/SBA-15. Thus, the sulfidation of the CoMo/SBA-15 catalyst is considerably retarded as compared with the other catalysts, in good agreement with XRD data indicating the formation of large-size $\beta\text{-CoMoO}_4$ crystallites (cf. Fig. 3). Considering the absence of correlation between the sulfidation degree of Co species and catalytic activity, the incomplete sulfidation of the Co species does not appear to be a serious drawback for catalytic activity, which is in good agreement with observations by Venezia et al. [53]. As the binding energies of Co 2p peaks are very high and characteristic of ionic Co^{2+} species interacting with the silicate surface, it is inferred that the fraction of non-sulfided cobalt does not interact with molybdenum and may therefore be responsible for Si–O–Co linkages rather than for the CoMoO_4 phase.

The XPS information on the active phase surface exposure is in line with that derived from the N_2 adsorption–desorption isotherms of the calcined precursors (*vide supra*). A plot of surface Mo/Si atomic ratio (from XPS) versus bulk Mo/Si atomic ratio (from

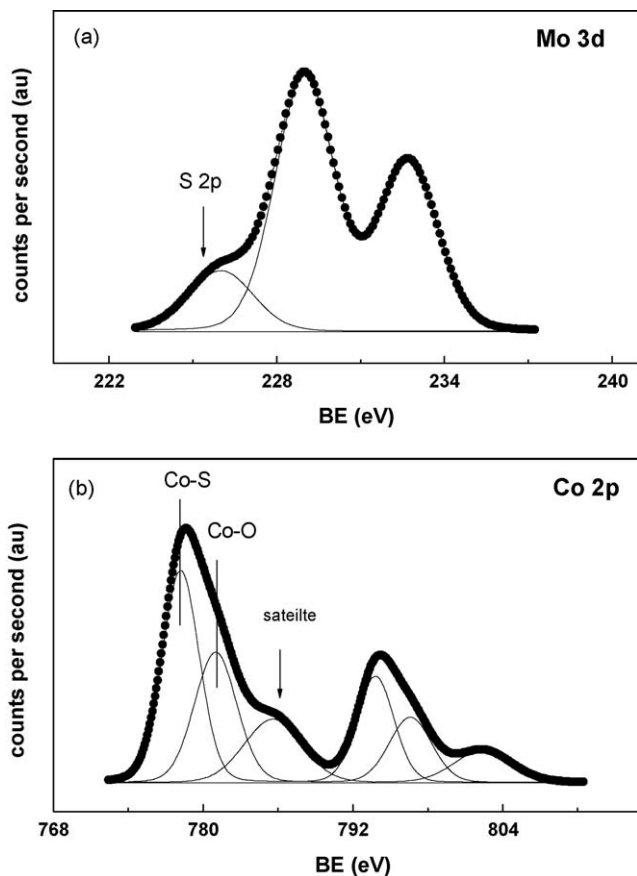


Fig. 13. Mo 3d (a) and Co 2p (b) and core levels XPS spectra of the spent CoMo/DMS-1 catalyst.

chemical analysis) clearly indicates that HMS and DMS-1-supported catalysts possess their molybdenum species mainly located within the inner porous structure (Fig. 14). This is in good agreement with their N_2 isotherms of the calcined precursors (Fig. 2) whose hysteresis loops indicate the presence of large mesopores formed by nanosize particles [54]. In comparison with the CoMo/HMS and CoMo/DMS-1, the CoMo/SBA-15 catalyst possesses a larger amount of molybdenum species located on the external support surface. Indeed, the type H1 hysteresis loop of its N_2 isotherm is characteristic of the mesoporous materials with metal-free 1-D cylindrical channels (Fig. 2). Finally, the N_2 isotherm of the calcined CoMo/SBA-16 showed a triangular H2-type adsorption-desorption hysteresis loop characteristic of mesoporous materials with cage-like pores (Fig. 2) indicating that its porous structure is metal-free [55]. In line with this, the XPS data indicate that molybdenum species are located on the external support surface of the CoMo/SBA-16 sample.

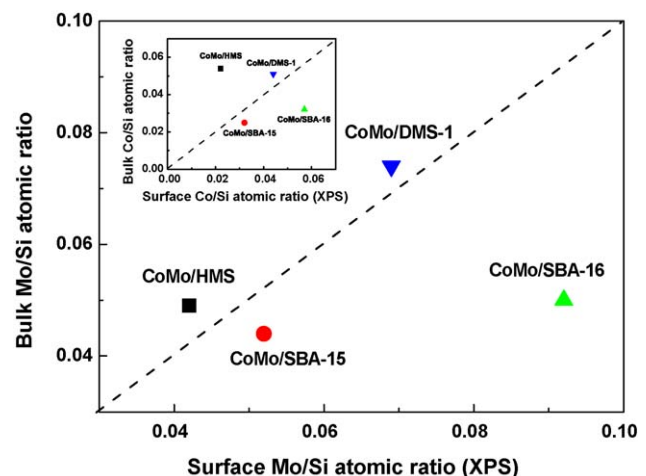


Fig. 14. Bulk Mo/Si atomic ratio of the calcined catalysts (from chemical analysis) versus surface Mo/Si atomic ratio of the sulfided catalysts (from XPS). Data corresponding to cobalt species are shown in inlet of this figure.

3.6. Influence of support morphology on coking behaviour

In this study, the nature and extent of coke formation on spent catalysts were studied by means of TG/DTG technique, measuring the weight losses of the coked catalysts upon oxidation in 20% O_2 /N₂ mixture. The TG and DTG profiles of the spent catalysts are displayed in Fig. 15. TPO results pointed out that carbon deposits strongly depend on the type of support. For all catalysts, the low temperature peak (ca. 375 °C) in TPO/DTG profiles lies within the region where metal sulfide phases are oxidized into the respective oxides. The weight loss corresponding to SO₂ evolution follows the trend: CoMo/DMS-1 (9.2%) > CoMo/HMS (6.3%) ≈ CoMo/SBA-16 (6.1%) > CoMo/SBA-15 (3.9%) indicating the largest stability of the latter catalyst.

For all catalysts, the DTG peaks at temperature > 500 °C are ascribed to the combustion of coke, being more graphitic as temperature increases. Considering the amount of coke formed during 5 h of on-stream operation, the observed trend is: CoMo/HMS (2.4%) > CoMo/SBA-15 ≈ CoMo/SBA-16 ≈ CoMo/DMS-1 (1.5–1.7%). Coke formation follows the same trend as total oxygen content after TOS = 5 h. This might indicate that the lowest activity of the HMS-supported catalyst is linked with the largest deactivation of its active sites by coke. No correlation is found between catalyst acidity and the extent of coke formation, indicating that coke reactivity depends basically on the catalyst structure, which is closely related to the morphology of the catalyst [56]. The genesis of coke in biomass upgrading by hydrotreating over the catalysts studied cannot be elucidated from these results. Further work is in progress in order to unravel the mechanism of coke formation on these catalysts.

Table 7

Binding energies (eV) and surface atomic ratios of the spent CoMo catalysts tested in the bio-liquid hydrotreating^a.

	CoMo/HMS	CoMo/SBA-15	CoMo/SBA-16	CoMo/DMS-1
Si 2p	103.3	103.4	103.4	103.4
Mo 3d _{5/2}	229.0	228.9	229.0	229.1
Co 2p _{3/2}	778.1 (53), 781.1 (47)	778.4 (49), 781.6 (51)	778.5 (44), 781.5 (56)	778.2 (47), 781.2 (53)
S 2p	162.1	161.9	162.0	162.0
Mo/Si	0.042	0.052	0.092	0.069
Co _{total} /Si	0.022	0.032	0.057	0.044
Co-Si/Si	0.012	0.016	0.025	0.021
S/(Mo + Co)	1.54	1.03	1.11	1.38
S/Si	0.097	0.093	0.182	0.157

^a Reaction conditions were: $T = 250$ °C; $P = 3$ MPa; WHSV_{bio-liquid} = 2.7 h⁻¹ and TOS = 5 h.

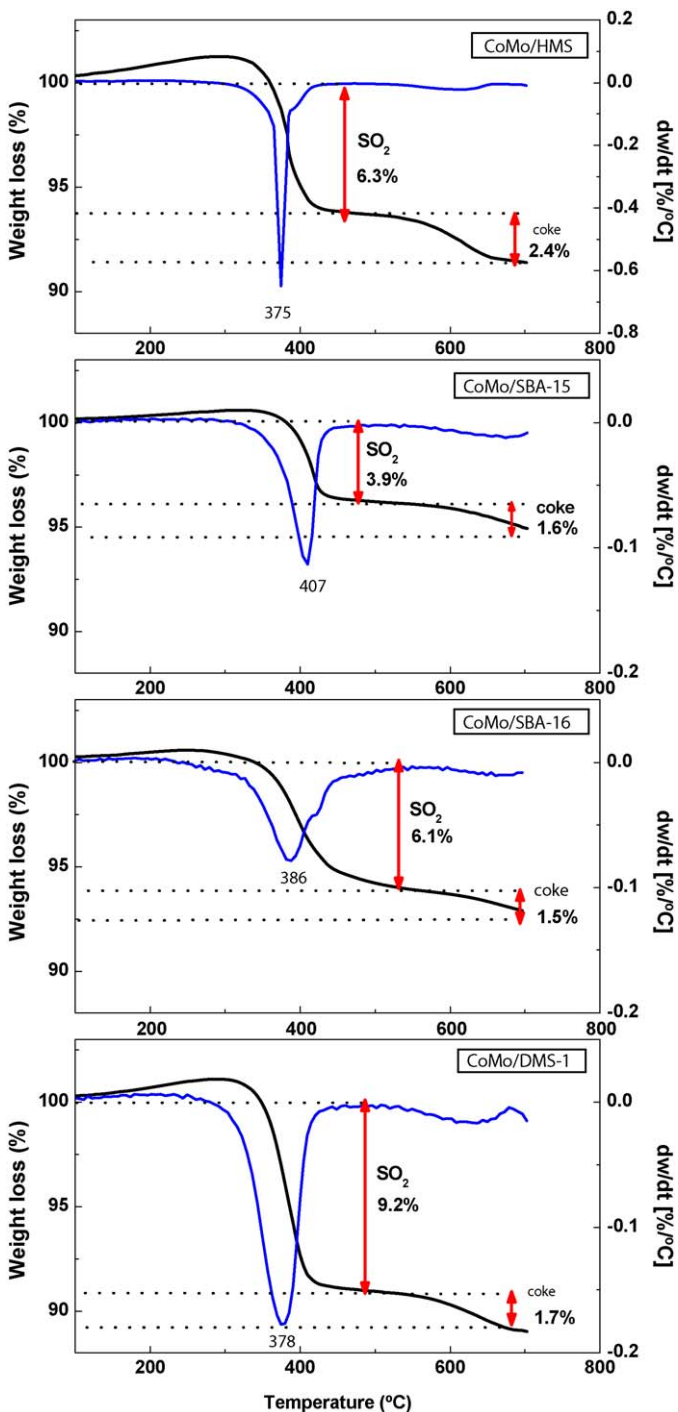


Fig. 15. TPO/TG profiles of the spent CoMo catalysts supported on mesoporous silica.

In short, the HDO activity of the catalysts studied is strongly influenced by the support acidity and much less so by the sulfidation degree of exposed cobalt species. During 5 h of on-stream reaction, the catalysts preserved their morphology, as was confirmed by low-angle XRD. For all catalysts, deactivation by coke was relatively low (1.5–2.4%). In general, the specific surface area of catalysts does not influence the HDO reaction in the biomass upgrading over CoMo catalysts. However, considering the yields of desired products (paraffin, alcohols or olefins), the cubic cage-structured SBA-16 is the most optimized material followed by SBA-15 (hexagonal pores and 1D channels) and DMS-1 (disordered

arrangement of pores). In this sense, the CoMo/SBA-16 catalyst is the most effective for alcohol production and the elimination of polyaromatics. The higher surface concentrations of Co and Mo species, as well as the easier sulfidation of Co species, contributed to the enhancement of the HDO reaction over the SBA-15, SBA-16 and DMS-1-supported catalysts with respect to the CoMo/HMS sample. TPR techniques confirmed the enhancement of metal oxide species reduction on the SBA-15, SBA-16 and DMS-1-supported catalysts with respect to the HMS-supported counterpart, suggesting a lower metal-support interaction on the three former catalysts.

4. Conclusions

Upgrading olive oil production by-products via hydrotreating was performed on sulfided CoMo catalysts supported on different mesoporous silicates (SBA-15, SBA-16, DMS-1, and HMS). The main conclusions derived from this work are the following:

- All CoMo catalysts supported on mesoporous silicates are much more active than a commercial NiMo/Al₂O₃ catalyst.
- The CoMo/SBA-16, CoMo/SBA-15 and CoMo/DMS-1 catalysts are more effective for oxygen removal and more selective toward desirable products than their CoMo/HMS counterpart.
- The HDO activity of the catalysts studied is strongly influenced by the support acidity and much less so by the sulfidation degree of surface cobalt species. All catalysts were stable during on-stream reaction, and deactivation by coke was relatively low (1.5–2.4%).
- The selectivity toward desired products is influenced by support morphology. The CoMo/SBA-16 catalyst is the most appropriate considering the formation of desirable products (paraffins and alcohols) and the removal of oxygen-containing products and polyaromatics (PAH). This sample is a good candidate for the first of a two-stage process to produce hydrocarbon fuels from biomass.

Acknowledgements

Financial support by the MICINN under Project ENE2007-67533-C02-01 is gratefully acknowledged. The authors acknowledge the assistance of Dr. M.A. Peña in TPO/TG measurements and Dr. J.M. Campos-Martin in the MS-GC analysis of products. Authors are grateful to Prof. P.L. Arias (University of the Basque Country, Bilbao, Spain) for fruitful discussions and providing the elemental analysis data of the feedstock.

References

- [1] I. Gandarias, V.L. Barrio, J. Requies, P.L. Arias, J.F. Cambra, M.B. Güemez, Int. J. Hydrogen Energy 33 (2008) 3485–3488.
- [2] The promotion of the Use of Biofuels or Related Other Renewable Fuels for Transport, EU Directive 2001/0265(COD), 25 February, 2003.
- [3] X. Dupain, D.J. Costa, C.J. Schaverien, M. Makkee, J.A. Moulijn, Appl. Catal. B: Environ. 72 (2007) 44–61.
- [4] G. Knothe, Fuel 84 (2005) 1059–1065.
- [5] E. Furimsky, Appl. Catal. A: Gen. 199 (2000) 147–190.
- [6] E.F. Iliopoulos, E.V. Antonakou, S.A. Karakoulia, I.A. Vasalos, A.A. Lappas, K.S. Triantafyllidis, Chem. Eng. J. 134 (2007) 51–57.
- [7] H. Topsøe, B.S. Clausen, F.E. Massoth, Hydrotreating Catalysts: Science and Technology, Springer, Germany, 1996, p. 22.
- [8] D.C. Elliott, G.G. Neuenschwander, in: A.V. Bridgwater, D.G.B. Boocock (Eds.), Developments in Thermochemical Biomass Conversion, Vol. 1, Blackie Academic & Professional, London, 1996, pp. 611–621.
- [9] R. Nava, R.A. Ortega, G. Alonso, C. Ornelas, B. Pawelec, J.L.G. Fierro, Catal. Today 127 (2007) 70–84.
- [10] R. Nava, B. Pawelec, J. Morales, R.A. Ortega, J.L.G. Fierro, Microporous Mesoporous Mater. 118 (2009) 189–201.
- [11] T.A. Zepeda, B. Pawelec, J.L.G. Fierro, T. Halachev, Appl. Catal. B: Environ. 71 (2006) 223–236.
- [12] T.A. Zepeda, T. Halachev, B. Pawelec, R. Nava, T. Klimova, G.A. Fuentes, J.L.G. Fierro, Chem. Mater. 17 (2005) 4062–4073.

- [13] T.A. Zepeda, T. Halachev, B. Pawelec, R. Nava, T. Klimova, G.A. Fuentes, J.L.G. Fierro, *Catal. Commun.* 7 (2006) 33–41.
- [14] B. Pawelec, S. Damyanova, R. Mariscal, J.L.G. Fierro, I. Sobrados, J. Sanz, L. Petrov, *J. Catal.* 223 (2004) 86–97.
- [15] F.A. Twaiq, R.A. Mohamed, S. Bhatia, *Microporous Mesoporous Mater.* 64 (2003) 95–107.
- [16] F.A. Twaiq, R.A. Mohamed, S. Bhatia, *Fuel Process. Technol.* 85 (2004) 1283–1300.
- [17] J. Adam, E. Antonakau, A. Lappas, M. Stöcker, M.H. Nilsen, A. Bouzga, J.E. Hustad, G. Øye, *Microporous Mesoporous Mater.* 96 (2006) 93–101.
- [18] J. Adam, M. Blazsó, E. Mészáros, M. Stöcker, M.H. Nilsen, A. Bouzga, J.E. Hustad, M. Grönli, G. Øye, *Fuel* 84 (2005) 1494–1502.
- [19] C.T. Kresge, M.E. Leonowicz, W.J. Roth, J.C. Vartuli, J.S. Beck, *Nature* 359 (1992) 710–712.
- [20] P.T. Tanev, M. Chibwe, T.J. Pinnavaia, *Nature* 368 (1994) 321–322.
- [21] P.T. Tanev, T.J. Pinnavaia, *Science* 267 (1995) 865–867.
- [22] D. Zhao, J. Feng, Q. Huo, N. Melosh, G.H. Fredrickson, B.F. Chmelka, G.D. Stucky, *Science* 279 (1998) 548–552.
- [23] W.J.J. Stevens, K. Lebeau, M. Mertens, G. Van Tendeloo, P. Cool, E.F. Vansant, *J. Phys. Chem. B* 110 (2006) 9183–9187.
- [24] R. Huirache-Acuña, B. Pawelec, E. Rivera-Muñoz, R. Nava, J. Espino, J.L.G. Fierro, Unpublished results.
- [25] J.C. Amezua, L. Lizama, C. Salcedo, I. Puente, J.M. Domínguez, T. Klimova, *Catal. Today* 107–108 (2005) 578–588.
- [26] D. Zhao, Q. Huo, J. Feng, B.F. Chmelka, G.D. Stucky, *J. Am. Chem. Soc.* 120 (1998) 6024–6036.
- [27] Y. Sakamoto, M. Kaneda, O. Teresaki, D. Zhao, J.M. Kim, G.D. Stucky, H.J. Shin, R. Ryoo, *Nature* 408 (2000) 449–453.
- [28] A. Bahamik, S. Samanta, N. Kishor Malet, *Microporous Mesoporous Mater.* 68 (2004) 29–35.
- [29] K. Flodström, V. Alfredsson, *Microporous Mesoporous Mater.* 59 (2003) 167–176.
- [30] W. Zhang, M. Froba, J. Wang, P.T. Tanev, T.J. Pinnavaia, *J. Am. Chem. Soc.* 118 (1996) 9164–9171.
- [31] L. Chen, T. Horiuchi, T. Mori, K. Maeda, *J. Phys. Chem. B* 103 (1999) 1216–1222.
- [32] C.D. Wagner, W.M. Riggs, L.E. Davis, J.F. Moulder, in: G.E. Muilenberg (Ed.), *Handbook of X-ray Photoelectron Spectroscopy*, Perkin Elmer Corp., Eden Prairie, MN, USA, 1979.
- [33] M. Samolada, A. Papafotica, I. Vasalos, *Energy Fuels* 14 (2000) 1161–1167.
- [34] K. Bourikas, Ch. Kordulis, A. Lycourghiotis, *Catal. Rev. Sci. Eng.* 48 (2006) 363–444.
- [35] S.J. Gregg, K.S.W. Sing (Eds.), *Adsorption, Surface Area and Porosity*, Academic Press, London, 1982.
- [36] F. Schüth, A. Wingen, J. Sauer, *Microporous Mesoporous Mater.* 44/45 (2001) 465–476.
- [37] A. Tuel, L.G. Hubert-Pfalzgraf, *J. Catal.* 217 (2003) 343–353.
- [38] M. Kruk, M. Jaroniec, C. Hyun Ko, R. Ryoo, *Chem. Mater.* 12 (2000) 1961–1968.
- [39] K. Segawa, K. Takahashi, S. Satoh, *Catal. Today* 63 (2000) 123–131.
- [40] K.M. Reddy, C. Song, *Catal. Today* 31 (1996) 137–144.
- [41] J.E. Herrera, D.E. Resasco, *J. Catal.* 221 (2004) 354–364.
- [42] J. Laine, J.L. Brito, F. Severino, *J. Catal.* 131 (1991) 385–393.
- [43] R. Nava, J. Morales, G. Alonso, C. Ornelas, B. Pawelec, J.I.G. Fierro, *Appl. Catal. A: Gen.* 321 (2007) 58–70.
- [44] R. Maggi, B. Delmon, in: G.F. Froment, B. Delmon, P. Grange (Eds.), *Hydrotreating and Hydrocracking of Oil Fractions*, Stud. Surf. Sci. Catal., Vol. 106, Elsevier Science B.V., Amsterdam, 1997, pp. 99–113.
- [45] R.L. Augustine, *Heterogeneous Catalysis for the Synthetic Chemist*, Marcel Dekker, New York, 1996, p. 462.
- [46] B. Pawelec, J.M. Campos-Martín, E. Cano-Serrano, R.M. Navarro, S. Thomas, J.L.G. Fierro, *Environ. Sci. Technol.* 39 (9) (2005) 3374–3381.
- [47] M. Bejblová, P. Zámostný, L. Červený, J. Čejka, *Appl. Catal. A: Gen.* 296 (2005) 169–175.
- [48] A. Guevara, R. Bacaud, M. Vrinat, *Appl. Catal. A: Gen.* 253 (2003) 515–526.
- [49] C.-H. Chen, H.-X. Li, M.E. Davis, *Microporous Mater.* 2 (1993) 17–26.
- [50] O.I. Şenol, T.-R. Viljava, A.O.I. Krause, *Catal. Today* 106 (2005) 186–189.
- [51] A.F.H. Sanders, A.M. de Jong, V.H.J. de Beer, J.A.R. van Veen, J.W. Niemantsverdriet, *Appl. Surf. Sci.* 144–145 (1999) 380–384.
- [52] D. Briggs, M.P. Seah (Eds.), *Practical Surface Analysis, Auger and X-ray Photoelectron Spectroscopy*, Wiley/Salle and Sauerländer, New York, 1990, p. 607.
- [53] A.M. Venezia, R. Murania, G. Pantaleo, G. Deganello, *J. Mol. Catal. A: Chem.* 71 (2007) 238–245.
- [54] K. Suzuki, K. Ikari, H. Imai, *J. Am. Chem. Soc.* 126 (2004) 462.
- [55] P.I. Ravikovich, A.V. Neimark, *Langmuir* 18 (2002) 1550.
- [56] C.L. Pieck, R.J. Verderone, E.J. Jablonski, J.M. Parera, *Appl. Catal.* 55 (1989) 1–10.